

PROGRESS REVIEW • OPEN ACCESS

STM imaging and electronic correlation in van der Waals ferromagnet Fe_3GeTe_2

To cite this article: Amir-Abbas Haghighirad *et al* 2025 *Jpn. J. Appl. Phys.* **64** 040805

View the [article online](#) for updates and enhancements.

You may also like

- [Magnetoresistance studies of two-dimensional \$\text{Fe}_3\text{GeTe}_2\$ nano-flake](#)
Xiangyu Zeng, Ge Ye, Shuyi Huang *et al.*
- [Antiferromagnetic coupling of van der Waals ferromagnetic \$\text{Fe}_3\text{GeTe}_2\$](#)
Dongseuk Kim, Sijin Park, Jinhwan Lee *et al.*
- [A sparse adaptive decision feedback equalization equipped with digital phase-locked loop on feedback filter for underwater acoustic communication with a fast-moving platform](#)
Yukihiro Kida, Mitsuyasu Deguchi and Takuya Shimura



ECS The Electrochemical Society
Advancing solid state & electrochemical science & technology

ECS UNITED

247th ECS Meeting
Montréal, Canada
May 18-22, 2025
Palais des Congrès de Montréal

**Register to
save \$\$
before
May 17**

Unite with the ECS Community



STM imaging and electronic correlation in van der Waals ferromagnet Fe₃GeTe₂

Amir-Abbas Haghighirad^{1*} , Ryo Ichikawa², Toshio Miyamachi^{3,4}, Haruki Ishii², Shun Akamatsu², Emiri Masui⁵, Osamu Ishiyama⁶, Hiroshi Iwayama⁷, Eiken Nakamura⁷, Toshihiko Yokoyama⁶, Eiichi Inami⁵, and Toyo Kazu Yamada^{2,8*} 

¹Institute for Quantum Materials and Technologies, Karlsruhe Institute of Technology, Kaiserstrasse 12, D-76131 Karlsruhe, Germany

²Department of Materials Science, Chiba University, 1-33 Yayoi-Cho, Inage-Ku, Chiba 263-8522, Japan

³Graduate School of Engineering and School of Engineering, Nagoya University, Furo-cho, Chikusa-ku, Nagoya, Aichi 464-8603, Japan

⁴Institute of Materials and Systems for Sustainability (IMaSS), Nagoya University, Nagoya, Aichi 464-8601, Japan

⁵School of Systems Engineering, Kochi University of Technology, 185 Miyanokuchi, Tosayamada, Kami, Kochi 782-8502, Japan

⁶Department of Materials Molecular Science, Institute for Molecular Science, Okazaki 444-8585, Japan

⁷UVSOR Synchrotron Facility, Institute for Molecular Science, Okazaki 444-8585, Japan

⁸Molecular Chirality Research Centre, Chiba University, 1-33 Yayoi-cho, Inage-Ku, Chiba 263-8522, Japan

*E-mail: amir-abbas.haghighirad@kit.edu; toyoyamada@faculty.chiba-u.jp

Received February 12, 2025; revised March 25, 2025; accepted March 31, 2025; published online April 24, 2025

Fe₃GeTe₂ is a van der Waals ferromagnet that has attracted significant attention due to its tuneable magnetic properties and potential applications in spintronic devices. In this work, we present a comprehensive study on high-quality Fe_{3-x}GeTe₂ (FGT) crystals using techniques including scanning tunneling microscopy (STM), atomic force microscopy (AFM), Kelvin probe force microscopy (KPFM), superconducting quantum interference device (SQUID) magnetometry, and X-ray magnetic circular dichroism (XMCD). STM and AFM reveal the atomic-scale surface morphology and layer-dependent structural features, highlighting the high crystallinity and terrace structures typical of van der Waals materials. KPFM measurements provide insights into the surface potential distribution and work function variations, indicating electronic structure modifications across different domains. Using the element-specific XMCD technique, we probe the local electronic characteristics of the magnetic ground state of FGT. From sum rule analysis, a significant difference between the orbital and spin moments is observed, leading to a notable spectroscopic splitting factor (*g*-factor). Our findings confirm notable contribution of both the Fe 3*d* and Ge-Te hybridized orbitals to the overall magnetic properties, shedding light on the microscopic mechanisms governing ferromagnetism in this material. This multi-technique approach provides a detailed understanding of the interplay between structure, electronic properties, and magnetism in FGT, paving the way for future applications in nanoscale magnetic devices. © 2025 The Author(s). Published on behalf of The Japan Society of Applied Physics by IOP Publishing Ltd

1. Introduction

van der Waals (vdW) materials have gained significant attention due to their unique properties and potential applications in spintronics and low-dimensional magnetism.¹⁻⁷ Among these, FGT stands out as a layered metallic ferromagnet that exhibits intrinsic ferromagnetism down to the monolayer limit.⁸⁻¹³ FGT belongs to the family of transition metal chalcogenides, characterized by weak interlayer vdW interactions and strong in-plane covalent bonding, enabling exfoliation into atomically thin layers. Bulk Fe₃GeTe₂ crystallizes in a hexagonal structure with space group *P6₃/mmc* and shows a relatively high Curie temperature of approximately 220 K,¹³ which can be further enhanced through doping or gating techniques. Its tuneable magnetic properties, coupled with high electrical conductivity, make it an ideal candidate for next-generation spintronic devices. Importantly, FGT exhibits strong perpendicular magnetic anisotropy,¹⁴⁻¹⁶ which is crucial for stable ferromagnetic order in low-dimensional systems. While the majority of studies have concentrated on bulk crystals, from a practical standpoint, it is imperative to understand how the electronic structure of the FGT surface is influenced during exfoliation processes. 2D magnets like FGT need to be reduced to the nanometer scale for the fabrication of nanoelectronic devices. However, this thinning process may induce bending or warping of the surface monolayer and/or alter the surface electronic properties due to the adsorption of impurities.

We have investigated the surface morphology and electronic properties of cleaved FGT single crystals in air and

ultra-high vacuum. We demonstrate how cleavage in air could alter the surface morphology and electronic properties of FGT using atomic force microscopy (AFM) and Kelvin probe force microscopy (KPFM). Second, we show how exfoliation in ultrahigh vacuum (UHV) modifies the surface morphology and electronic structures by employing scanning tunneling microscopy and spectroscopy (STM/STS) at 78 K and explore the ferromagnetic properties of FGT using X-ray magnetic circular dichroism (XMCD) in UHV.

2. Methods and materials

2.1. Crystal growth and chemical analysis

Single crystals of Fe_{3-x}GeTe₂ were grown by chemical vapor transport (CVT) using I₂ or TeCl₄ as a transport agent^{17, 18}. High purity elemental reagents, Ge (Merck, 99.999%) and Te (*G*-Materials, 99.999%) were mixed in a 3.1:1:2 molar ratio and thoroughly ground in an argon-filled glove box (O₂ content is <0.2 ppm) and sealed in an evacuated (at ~10⁻⁵ mbar) fused silica ampule. The loaded ampule containing ~3.0 g of mixed elemental reagents and ~95 mg TeCl₄, were placed in a two-zone-furnace. The source temperature was set at ~750 °C, and the sink temperature was set to 690 °C. These conditions were maintained for 12 d. Shiny crystals with hexagonal facets [see *inset* in Fig. 1(a)] were collected from the deposition side of the fused silica ampule. The crystals can easily be cleaved using scotch tape in order to get a nicely fresh surface. The chemical composition of the crystals was determined using energy dispersive X-ray spectroscopy (EDS) in a COXEM



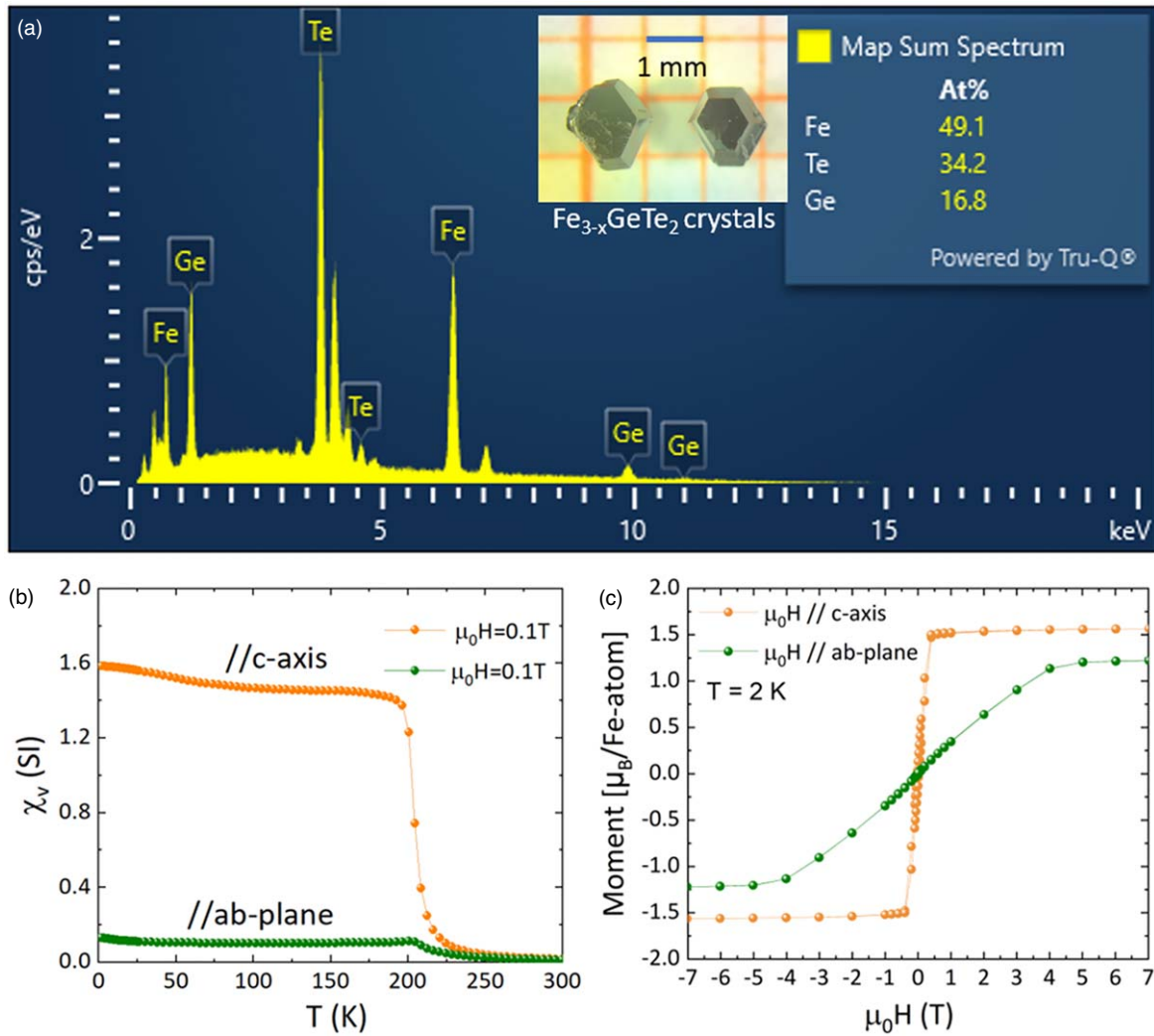


Fig. 1. Electron probe microanalysis and SQUID magnetometry of $\text{Fe}_{3-x}\text{GeTe}_2$. (a) EDX spectrum of surface of a FGT single crystal—*inset*: FGT single crystals (b) Magnetic susceptibility measured as a function of temperature in field-cooled (FC) condition (c). Magnetization as a function of field at 2 K.

EM-30plus electron microscope equipped with an Oxford silicon-drift-detector (SDD) and AZtecLiveLite-software package. EDS revealed a quantitative elemental composition of $\text{Fe}:\text{Ge}:\text{Te} = 2.92:1:2.04$, respectively. The EDS spectrum of the quantitative elemental mapping is shown in Fig. 1(a). In this study, we used six FGT crystals, all prepared using the same growth conditions: the first for AFM/KPFM, the second for STM/STS, the third for SQUID, and the remaining ones for XMCD measurements.

2.2. Magnetic characterization of FGT

Magnetic measurements were performed using a superconducting quantum interference device (SQUID) magnetometer in fields up to 7 T. Magnetic volume susceptibility $\chi_v(T)$ versus temperature in $H = 0.1\text{ T}$ (field-cooled) and the isothermal magnetization versus field $M(H)$ at 2 K of a FGT single crystal are shown in Figs. 1(b) and 1(c), respectively. For both magnetic susceptibility and isothermal magnetization, the data were measured with the magnetic field along $H \parallel ab$ and $H \parallel c$.

2.3. Home-built low-temperature UHV STM setup

STM measurements were performed using home-built UHV-STM equipment consisting of STM, preparation, and deposition chambers.^{19–22} The base pressures of each chamber were below $5.0 \times 10^{-8}\text{ Pa}$, $2.0 \times 10^{-8}\text{ Pa}$, and $1.0 \times 10^{-7}\text{ Pa}$, respectively. Samples and STM tips were transferred between

chambers using transfer rods without breaking the UHV. Gate valves separated each chamber. A UHV cryostat (CryoVAC) in the STM chamber was used to cool down the STM setup. We used sharp tungsten tips as STM probe tips utilizing both conventional chemical etching and flame etching, producing a sharp tip within 3 s.^{23–26}

2.4. STM/STS measurements

A home-built STM combined with the Nanonis SPM controller BP4 obtained topographic images of sample surfaces in a constant current mode since the tunneling current (I) detected by the tip is exponentially proportional to the tip–sample separation (z) via $\exp(-(8m(\Phi \pm eV/2))^{1/2} z/\hbar)$, where m : electron mass, \hbar : Planck constant, Φ : apparent barrier height between tip and sample, and V : set point sample bias voltage,^{27,28} we can measure the surface corrugations with atomic resolution.

STS measures sample surface local density of states (LDOS).^{27,28} I , as a function of sample bias voltages (typically, from -2 to $+2\text{ V}$), was measured under feedback off condition (one single curve was measured within 50–200 ms) by fixing the tip–sample separation ($z = z_c$), which was determined by the setpoint voltage (V_s) and the current (I_s). The obtained $I(V)$ curves were numerically differentiated, and differential conductance (dI/dV) curves were obtained: $dI/dV \sim \rho_s$

$(-8m(\Phi \pm eV/2))^{1/2} z/\hbar$). The STM/STS data were analyzed using WSxM 5.0 Develop 10.2 software and Gwyddion 2.53.²⁹⁾

2.5. AFM/KPFM measurements

Surface topographies and surface potentials of the samples were characterized using AFM under ambient conditions (Cypher VRS, Oxford Instruments). A Ti/Ir coated silicon cantilever (ASYELEC-01-R2, Oxford Instruments) has externally oscillated via photothermal excitation (Blue Drive). Surface topographies were imaged in tapping mode. KPFM imaging was performed using a frequency-modulation (FM)-sideband technique,³⁰⁾ with the compensation voltage applied to the cantilever.

2.6. UHV cleavage

We used FGT crystals with typical dimensions of 1–3 mm in size and 0.1–1.0 mm in thickness. These TMD crystals were typically adhered to a metal substrate; in this case, we used a Molybdenum sample plate with a conductive epoxy (H20E). Care had to be taken to ensure the adhesive did not extend beyond the bottom of the crystal. Although vdW materials can provide atomically flat and clean surfaces through tape cleaving in air, however, our STM tests on such surfaces revealed impurity adsorption from the air, which could damage and modify the material's intrinsic properties. To mitigate this, we introduced the sample through a load lock chamber. We performed the cleavage in the UHV pre-chamber and then transferred the sample into the STM or XMCD while maintaining UHV conditions. The FGT single crystal was cleaved using blue tape (Nitto ELP-BT-150E-CM), which was affixed to the apex of the transfer rod. First, the tape was gently pressed against the surface of the crystal; then, the sample was moved laterally while simultaneously pulling out the rod, thereby achieving the peeling operation.

2.7. XAS and XMCD measurements

XAS and XMCD measurements were conducted at BL4B of the UVSOR Synchrotron Facility, Institute for Molecular Science, Japan.^{31,32)} FGT samples were placed on a copper plate. After tape cleavage in a vacuum of 7×10^{-6} Pa, the sample was transferred into the XMCD cryostat sample stage. All XAS and XMCD measurements were performed at 6 K under UHV conditions. Circularly polarized light was directed onto the sample, exciting photoelectrons and generating a positively charged surface. The adsorption current (I), proportional to the number of photoelectrons, was measured from the ground to the sample. The X-ray initially passed through the gold mesh, where the adsorption current (I_0) was detected. Adsorption spectra were obtained by calculating the ratio of I/I_0 .

3. Results and discussion

3.1. Magnetic characterization of FGT

As reported earlier,¹¹⁾ the $\chi_v(T)$ shows a clear ferromagnetic transition with a $T_c \sim 205$ K. The $\chi_v(T)$ differs strongly depending on the direction of the applied magnetic field (i.e. $\chi_v(T)$ and is approximately 15 times larger at $H \parallel c$ compared to $H \parallel ab$). This clearly indicated that the magnetic easy axis is along the crystallographic c -axis. This is further supported by the results of $M-H$ loops at 2 K, as shown in Fig. 1(c). Saturation magnetization is obtained at a very large field of $H > 4$ T when $H \parallel ab$. On the contrary, saturation magnetization is attained already at

0.5 T when $H \parallel c$. The magnetic coercive field of FGT is 0.03 T, and the average ferromagnetic moment is $m_s = 1.58\mu_B/\text{Fe-ion}$. Furthermore, the high-temperature region (265–300 K) of $\chi_v(T)$ was fitted with Curie–Weiss law and determined the paramagnetic effective moment of $P_{\text{eff}} = 2.85\mu_B/\text{Fe-ion}$. Thus, the ratio of the paramagnetic effective moment P_{eff} and the spin moment is $P_{\text{eff}}/m_s = 1:8$,

which might reflect the itinerant nature of the ordered moment. In summary, our measurements indicate that FGT is a strong ferromagnet which is exotic in nature. Our measurements did not show any indication of antiferromagnetic coupling in the system.

3.2. FGT surfaces structures in air

Figure 2(a) shows an optical microscope image of a $\text{Fe}_{2.9}\text{GeTe}_2$ crystal, which is a few mm in size and approximately 0.1 mm in thickness. Despite storing the sample in a vacuum desiccator after CVT growth, the initially mirror-like surface degraded and appeared dull. The magnified image in Fig. 2(a) reveals numerous scratches and darker regions on the surface. Figure 2(b) displays the AFM topographic image and the work function map acquired via KPFM from the same region of the crystal surface. The surface exhibits flat terraces that appear to be delaminating in certain regions, resulting in hole-like pitches with depth variations of 5–10 nm. The work function map indicates that the terrace and hole areas exhibit distinct work functions (with an approximate 0.2 eV difference), with brighter regions corresponding to higher work functions and darker regions to lower ones. The experimental observations in Figs. 2(a) and 2(b) suggest that the FGT crystal undergoes degradation compared to graphite, exhibiting notable alterations in surface morphology and electronic structure from its original state.

We cleaved the surface using adhesive tape [Fig. 2(c)]. Post-cleavage, the FGT surface exhibited a pristine, highly reflective appearance [Fig. 2(d)]. The magnified optical microscopy image in Fig. 2(d) shows a marked reduction in scratches and darker spots. AFM and KPFM images of this surface, depicted in Fig. 2(d), reveal a substantial enhancement in surface quality. Figure 1(e) illustrates atomically flat terraces (with roughness less than 100 pm), each extending beyond 1000 nm, and a uniform work function across the entire surface. Thus, although the FGT crystal is susceptible to oxidation, tape cleavage effectively restores a clean, pristine surface.

The experimental findings in Fig. 2 suggest that maintaining UHV conditions significantly diminishes impurity levels, thus facilitating the preservation of the intrinsic surface state over extended periods. Consequently, we performed surface morphology and electronic structure measurements in UHV. Nevertheless, we encountered further challenges in achieving an atomically flat and clean FGT surface through tape cleavage in UHV.

3.3. FGT surface structures in UHV

The FGT crystal surface, after tape cleavage in UHV, reveals several FGT films, approximately 1 mm in size, distributed across the surface, with their edges slightly curled. The surface morphology of the FGT sample was examined without disrupting UHV conditions following the tape cleavage. The sample was promptly transferred to the STM

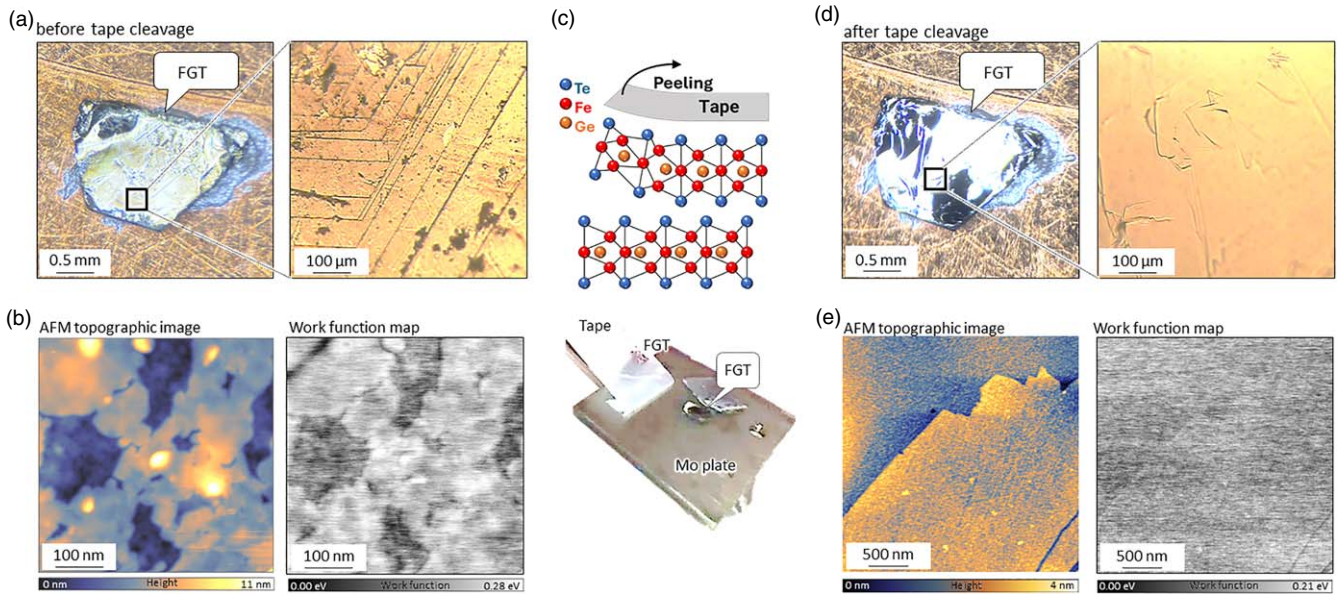


Fig. 2. Comparing surface structures before and after the tape cleaving in air. (a) Optical microscopy images of FGT crystal fixed on a Mo sample plate using the Epoxy H20E glue before the tape cleavage. (b) AFM topographic image and simultaneously obtained work function map (500 nm × 500 nm at 300 K in air). (c) Schematic model during the tape cleaving of the FGT surface. The lower panel shows how we performed the cleavage of the FGT fixed on the Mo plate. (d) Optical microscopy images of FGT crystal after the tape cleavage. (e) AFM topographic image and simultaneously obtained work function map (3000 nm × 3000 nm at 300 K in air).

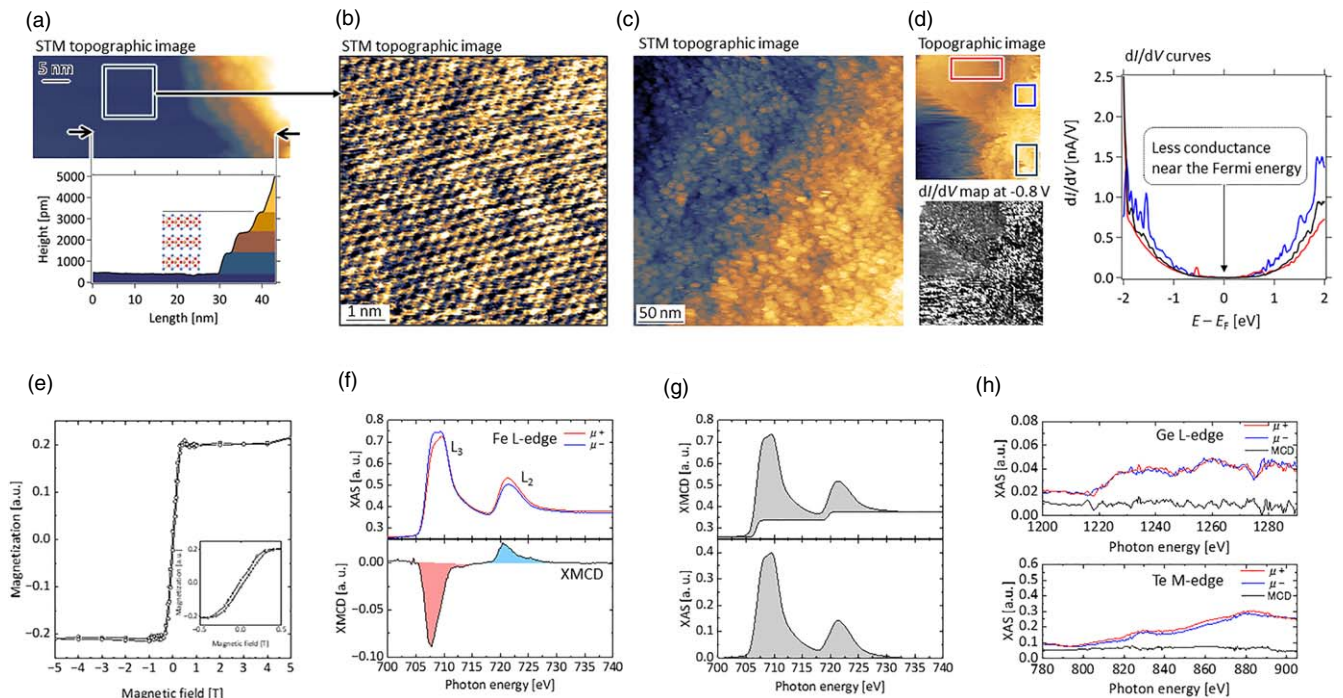


Fig. 3. STM/STS and XMCD measurements at cryogenic temperatures in UHV on FGT surfaces after the tape cleavage in UHV. (a) STM topographic images at 78 K in UHV. The left panel (50 × 20 nm², $V_s = -0.5$ V, $I_t = 100$ pA) shows several atomic terraces on the surface. The height profile between the arrows denotes FGT monolayer film stacking. (b) The magnified image (10 × 10 nm², $V_s = -50$ mV, $I_t = 4$ pA) within the box represents atomic alignment on the surface, showing a hexagonal symmetry. (c) Wide-scanned STM topographic image obtained on the same FGT crystal surface but in different areas (300 × 300 nm², $V_s = -1$ V, $I_t = 100$ pA) showing a non-atomically flat surface. (d) STM topographic image and simultaneously measured dI/dV map (99 × 99 nm², $V_s = -2$ V, $I_t = 500$ pA). dI/dV curves obtained at three different areas marked by the boxes in the topographic image. (e) M - B loop at 6 K in UHV: magnetization variation as a function of applied external magnetic field (out-of-plane, within $B = \pm 5$ T). (f) Fe $L_{2,3}$ XAS (μ_+ , μ_-) and XMCD. (g) The background step function was fitted using the Fermi functions, as shown in the lower panel. (h) XAS and MCD spectra for the Ge L and Te M edges.

stage, which was operated at 78 K. The STM tip was positioned over one of the flat FGT films, and STM measurements were subsequently conducted.

The STM topographic image in Fig. 3(a) displays atomically flat terraces approximately 20–30 nm wide, with step

heights around 900 pm, corresponding to a single quintuple layer (SQL) of FGT. The height profile in Fig. 3(a) indicates a stacking of three SQLs. A magnified view of the marked region on the right-hand side of Fig. 3(b) reveals hexagonal symmetry in the alignment of surface atoms.

However, achieving atomically flat terraces with a 20–30 nm width proved challenging. Instead, most surface regions exhibited features similar to those in Fig. 3(c), where SQL steps are spaced a few nanometers apart, resulting in a non-flat surface. Figure 3(c) shows a large-scale STM topographic image (300 nm × 300 nm), revealing numerous small, patch-like terraces distributed across the surface. To investigate the electronic structure of the surface, STS measurements were performed [Fig. 3(d)]. The differential conductivity, dI/dV , is directly proportional to the sample's LDOS. Figure 3(d) displays an STM topographic image alongside the dI/dV maps obtained at an energy value of $E - E_F = -0.8$ eV, corresponding to the occupied states at -0.8 eV below the Fermi energy, representing local variations across the surface. In the dI/dV maps, brighter regions correspond to higher LDOS, while darker regions represent lower LDOS. dI/dV curves obtained from three distinct areas, marked by red, blue, and black boxes in the topographic image, show that all three curves demonstrate an exponential increase with energy, with less conductance ($dI/dV \approx 0.0$ nA V⁻¹) near the Fermi energy. Critical remarks are that depending on the cleavage, such a non-flat area could produce non-uniform electronic structures on the surface using tape cleavage in UHV.

We further examined the magnetic properties of the surface using XAS and XMCD. Figure 3(e) shows the magnetization as a function of the applied external magnetic field within ±5 Tesla (T) in the out-of-plane direction, with X-ray circularly polarized light incident from the normal direction. The inset highlights the region near zero Tesla, indicating a coercive field of approximately 23 mT. This hysteresis loop confirms that the FGT sample surface exhibits ferromagnetic properties, with the easy axis aligned parallel to the out-of-plane direction.

Figure 3(f) presents XAS curves obtained from the Fe L_{2,3} edges under circularly polarized light (μ_+ , μ_-), showing a clear difference between the two curves. The step-like background was subtracted from the curves [Fig. 3(g)], revealing the peaks. The XMCD spectrum is shown in Fig. 3(f), confirming the magnetization of the Fe atoms. Using the XMCD sum rule,^{10,33} we can roughly estimate the spin magnetic moment as $m_{\text{spin}} + 7\langle T_z \rangle \sim 1.84\mu_B$, where $\langle T_z \rangle$ represents the spin-quadrupole contribution to the sum rule, and the orbital magnetic moment is $m_{\text{orbital}} \sim 0.15\mu_B$. XMCD signals for the Ge and Te atoms were also examined [Fig. 3(h)]. These signals are nonzero, suggesting that the Ge and Te atoms neighboring the Fe atoms are likely spin-polarized due to their proximity to the ferromagnetic Fe.

We have considered the $3d^6$ electronic configuration for Fe in FGT. Since the total $3d$ iron moment is $m_{\text{tot}} = m_S + m_L$, we use the total moment measured by bulk magnetization to calculate the spin moment. In our study, we report a slightly higher orbital moment, $0.15\mu_B$, compared to $0.10\mu_B$ observed by Zhu et al.¹⁰ Additionally, the spin moment in this work is $1.85\mu_B$, which is higher than the previously reported value of $1.48\mu_B$, likely due to differences in Fe deficiency. Additionally, the temperature difference (6 K versus 45 K) could contribute to the observed discrepancies, as orbital moments can be temperature-dependent. Both studies confirm the presence of significant spin–orbit coupling and highlight Fe $3d$ and Ge–Te hybridization effects.

4. Conclusions

This comprehensive study provides crucial insights into the interplay between the atomic-scale structure, electronic properties, and magnetic behavior of the vdW ferromagnet Fe₃GeTe₂ (FGT) using multiple characterization techniques, including STM/STS, AFM/KPFM, SQUID and XMCD. The research highlights the influence of exfoliation methods and environmental conditions on the surface morphology and electronic properties of FGT. XMCD results have confirmed that ferromagnetic properties are strongly influenced by both Fe $3d$ and Ge–Te hybridized orbitals, with measurable spin–orbit coupling enhancing the magnetic anisotropy. The detailed surface analysis highlights the challenges of achieving atomically flat surfaces, which are critical for realizing nanoscale spintronic devices. This multi-technique approach not only advances our understanding of vdW ferromagnets but also paves the way for their integration into next-generation nanoscale magnetic and spintronic applications.

Author contributions

A.A.H. and T.K.Y. designed and led the study and co-wrote the original manuscript, and all co-authors meticulously reviewed and corrected it. A.A.H. synthesized and evaluated the FGT crystals. STM/STS measurements were conducted by S.A., H.I., R.I., and T.K.Y. AFM/KPFM measurements were performed by S.A. and E.I. XMCD measurements were performed with R. I., T. M., H. I., O. I., H. I., E. N., T. Y., and T. K. Y.

Acknowledgments

This work was supported by JSPS KAKENHI Grant Nos. 17K19023, 19H05789, 20H02697, 21H01812, and 23H02033, the Murata Science Foundation, the Shorai Foundation for Science and Technology, TEPCO Memorial Foundation, Casio Science Promotion Foundation, and Toshiaki Ogasawara Memorial Foundation. A part of this work was conducted at the BL4B of UVSOR Synchrotron Facility, Institute for Molecular Science, supported by Advanced Research Infrastructure for Materials and Nanotechnology in Japan (JPMXP1223MS2002) of the Ministry of Education, Culture, Sport, Science and Technology (MEXT), Japan. A.A.H. acknowledges support of the Deutsche Forschungsgemeinschaft (DFG; German Research Foundation) under CRC/TRR 288 (Project No. B03).

ORCID iDs

Amir-Abbas Haghighirad  <https://orcid.org/0000-0003-4723-4966>

Toyo Kazu Yamada  <https://orcid.org/0000-0001-5185-6472>

- 1) H. Li, S. Ruan, and Y. Zeng, “Intrinsic van der Waals magnetic materials from bulk to the 2D limit: new frontiers of spintronics,” *Adv. Mater.* **31**, 1900065 (2019).
- 2) S. Jiang, J. Shan, and K. F. Mak, “Electric-field switching of two-dimensional van der Waals magnets,” *Nat. Mater.* **17**, 406 (2018).
- 3) K. S. Burch, D. Mandrus, and J.-G. Park, “Magnetism in two-dimensional van der Waals materials,” *Nature* **563**, 47 (2018).
- 4) D. L. Duong, S. J. Yun, and Y. H. Lee, “van der Waals layered materials: opportunities and challenges,” *ACS Nano* **11**, 11803 (2017).

- 5) K. S. Novoselov, A. Mishchenko, A. Carvalho, and A. H. Castro Neto, "2D materials and van der Waals heterostructures," *Science* **353**, aac9439 (2016).
- 6) Y. Liu, N. O. Weiss, X. Duan, H.-C. Cheng, Y. Huang, and X. Duan, "van der Waals heterostructures and devices," *Nat. Rev. Mater.* **1**, 16042 (2016).
- 7) P. Ajayan, P. Kim, and K. Banerjee, "Two-dimensional van der Waals materials," *Phys. Today* **69**, 38 (2016).
- 8) A. F. May, C. A. Bridges, and M. A. McGuire, "Physical properties and thermal stability of $\text{Fe}_{5-x}\text{GeTe}_2$ single crystals," *Phys. Rev. Mater.* **3**, 104401 (2019).
- 9) W. Jiang, G. Chen, K. Liu, J. Zang, S. G. E. Te Velthuis, and A. Hoffmann, "Skyrmions in magnetic multilayers," *Phys. Rep.* **704**, 1 (2017).
- 10) J.-X. Zhu et al., "Electronic correlation and magnetism in the ferromagnetic metal Fe_3GeTe_2 ," *Phys. Rev. B* **93**, 144404 (2016).
- 11) A. F. May, S. Calder, C. Cantoni, H. Cao, and M. A. McGuire, "Magnetic structure and phase stability of the van der Waals bonded ferromagnet $\text{Fe}_{3-x}\text{GeTe}_2$," *Phys. Rev. B* **93**, 014411 (2016).
- 12) N. León-Brito, E. D. Bauer, F. Ronning, J. D. Thompson, and R. Movshovich, "Magnetic microstructure and magnetic properties of uniaxial itinerant ferromagnet Fe_3GeTe_2 ," *J. Appl. Phys.* **120**, 083903 (2016).
- 13) V. Y. Verchenko, A. A. Tsirlin, A. V. Sobolev, I. A. Presniakov, and A. V. Shevelkov, "Ferromagnetic order, strong magnetocrystalline anisotropy, and magnetocaloric effect in the layered telluride $\text{Fe}_{3-6}\text{GeTe}_2$," *Inorg. Chem.* **54**, 8598 (2015).
- 14) Q. Li et al., "Patterning-induced ferromagnetism of Fe_3GeTe_2 van der Waals materials beyond room temperature," *Nano Lett.* **18**, 5974 (2018).
- 15) H. L. Zhuang, P. R. C. Kent, and R. G. Hennig, "Strong anisotropy and magnetostriction in the two-dimensional stoner ferromagnet Fe_3GeTe_2 ," *Phys. Rev. B* **93**, 134407 (2016).
- 16) H.-H. Yang et al., "Magnetic domain Walls of the van der Waals material Fe_3GeTe_2 ," *2D Mater.* **9**, 025022 (2022).
- 17) M. Corasaniti, R. Yang, K. Sen, K. Willa, M. Merz, A. A. Haghighirad, M. Le Tacon, and L. Degiorgi, "Electronic correlations in the van der Waals ferromagnet Fe_3GeTe_2 revealed by its charge dynamics," *Phys. Rev. B* **102**, 161109 (2020).
- 18) H.-H. Yang et al., "Magnetic domain walls of the van der Waals material Fe_3GeTe_2 ," *2D Materials* **9**, 025022 (2022).
- 19) F. Nishino et al., "Reversible sliding motion by hole-injection in ammonium-linked ferrocene, electronically decoupled from noble metal substrate by crown-ether template layer," *Small* **12**, 2408217 (2024).
- 20) T. K. Yamada, R. Nemoto, H. Ishii, F. Nishino, Y.-H. Chang, C.-H. Wang, P. Krüger, and M. Horie, "Designing 2D stripe winding network through crown-ether intermediate ullmann coupling on Cu(111) surface," *Nanoscale Horiz.* **9**, 718 (2024).
- 21) T. K. Yamada, R. Nemoto, F. Nishino, T. Hosokai, C.-H. Wang, M. Horie, Y. Hasegawa, S. Kera, and P. Krüger, "On-surface growth of transition-metal cobalt nanoclusters using a 2D crown-ether array," *J. Mater. Chem. C* (2024).
- 22) T. K. Yamada, S. Kanazawa, K. Fukutani, and S. Kera, "Growth of transition-metal cobalt nanoclusters on 2D covalent organic frameworks," *J. Phys. Chem. C* **128**, 1477 (2024).
- 23) C. G. Ayani, F. Calleja, I. M. Ibarburu, P. Casado Aguilar, N. K. M. Nazriq, T. K. Yamada, M. Garnica, A. L. Vázquez De Parga, and R. Miranda, "Switchable molecular functionalization of an STM tip: from a Yu-Shiba-Rusinov tip to a Kondo tip," *Nanoscale* **14**, 15111 (2022).
- 24) T. Yamaguchi, E. Inami, Y. Goto, Y. Sakai, S. Sasaki, T. Ohno, and T. K. Yamada, "Fabrication of tungsten tip probes within 3 s by using flame etching," *Rev. Sci. Instrum.* **90**, 063701 (2019).
- 25) Y. Goto, R. Suizu, Y. Noguchi, and T. K. Yamada, "Oxidative vaporization etching for molybdenum tip formation in air," *Appl. Surf. Sci.* **542**, 148642 (2021).
- 26) T. K. Yamada, T. Abe, N. M. K. Nazriq, and T. Irisawa, "Electron-bombarded (110)-oriented tungsten tips for stable tunneling electron emission," *Rev. Sci. Instrum.* **87**, 033703 (2016).
- 27) V. A. Ukraintsev, "Data evaluation technique for electron-tunneling spectroscopy," *Phys. Rev. B* **53**, 11176 (1996).
- 28) Y. Yamagishi, S. Nakashima, K. Oiso, and T. K. Yamada, "Recovery of nanomolecular electronic states from tunneling spectroscopy: LDOS of low-dimensional phthalocyanine molecular structures on Cu(111)," *Nanotechnol.* **24**, 395704 (2013).
- 29) I. Horcas, R. Fernández, J. M. Gómez-Rodríguez, J. Colchero, J. Gómez-Herrero, and A. M. Baro, "WSXM: a software for scanning probe microscopy and a tool for nanotechnology," *Rev. Sci. Instrum.* **78**, 013705 (2007).
- 30) A. Axt, I. M. Hermes, V. W. Bergmann, N. Tausendpfund, and S. A. L. Weber, "Know your full potential: quantitative Kelvin probe force microscopy on nanoscale electrical devices," *Beilstein J. Nanotechnol.* **9**, 1809 (2018).
- 31) T. Miyamachi et al., "Spin reorientation and large magnetic anisotropy of metastable bcc Co Islands on Au(001)," *Phys. Rev. B* **90**, 174410 (2014).
- 32) H. Ono et al., "Intermolecular interaction induced magnetic decoupling at an organic-inorganic interface," *J. Phys. Chem. C* **127**, 23935 (2023).
- 33) S. Stepanow, A. Mugarza, G. Ceballos, P. Moras, J. C. Cezar, C. Carbone, and P. Gambardella, "Giant spin and orbital moment anisotropies of a Cu-phthalocyanine monolayer," *Phys. Rev. B* **82**, 014405 (2010).